Draft version October 15, 2010
Preprint typeset using LaTeX style emulateapj v. 5/25/10

arXiv:1010.1577v2 [astro-ph.CO] 14 Oct 2010

CONSTRAINING HALO OCCUPATION PROPERTIES OF X-RAY AGNS USING CLUSTERING OF *CHANDRA* SOURCES IN THE BOÖTES SURVEY REGION

S. Starikova[1,2], R. Cool[3,4,5], D. Eisenstein[2], W. Forman[2], C. Jones[2], R. Hickox[6,7], A. Kenter[2], C. Kochanek[8], A. Kravtsov[9], S. S. Murray[10,2], A. Vikhlinin[2,11]

Draft version October 15, 2010

ABSTRACT

We present the most precise measurement to date of the spatial clustering of X-ray selected AGNs using a sample derived from the *Chandra* X-ray Observatory survey in the Bootes field. The real-space two-point correlation function over a redshift interval from $z = 0.17$ to $z \sim 3$ is well described by the power law, $\xi(r) = (r/r_0)^{-\gamma}$, for comoving separations $r \lesssim 20\,h^{-1}$ Mpc. We find $\gamma = 1.97 \pm 0.09$ and r_0 consistent with no redshift trend within the sample (varying between $r_0 = 5.4 \pm 0.5\ h^{-1}$ Mpc for $\langle z \rangle = 0.37$ and $r_0 = 7.0 \pm 0.8\ h^{-1}$ Mpc for $\langle z \rangle = 1.28$). Further, we are able to measure the projections of the two-point correlation function both on the sky plane and in the line of sight. We use these measurements to show that the *Chandra*/Boötes AGNs are predominantly located at the centers of dark matter halos with the circular velocity $v_{\rm max} > 310\,{\rm km\ s^{-1}}$ or $M_{180} > 3.7 \times 10^{12}\,h^{-1}\,M_\odot$, and tend to *avoid* satellite galaxies in halos of this or higher mass. The halo occupation properties inferred from the clustering properties of *Chandra*/Boötes AGNs — the mass scale of the parent dark matter halos, the lack of significant redshift evolution of the clustering length, and the low satellite fraction — are broadly consistent with the Hopkins et al. (2006) scenario of quasar activity triggered by mergers of similarly-sized galaxies.

1. INTRODUCTION

Direct observations of host galaxies of the high-redshift active galactic nuclei are hard or impossible with the current instrumentation, except for highly obscured or low-luminosity objects. Studies of the AGN clustering properties are thus a unique source of information on the AGN hosts and their environment. At low redshifts, the supermassive black holes exist at the centers of most low-redshift galaxies, and there is a tight correlation between the SMBH mass and the properties of the bulges of host galaxies (Magorrian et al. 1998; Ferrarese & Ford 2005; Gebhardt et al. 2000). This suggests that most galaxies hosted an AGN at some point in their evolution, and that AGNs at each redshift are stochastic "markers" of a population of galaxies in which the conditions are favorable for accretion of matter onto the central SMBH. Through matching the clustering properties of AGNs to those of dark matter halos, or with those of different types of galaxies, or with those of AGNs of different types, we can determine the typical mass scale of the AGN hosts, their morphological type, and determine whether different types of AGNs are hosted in the same type of objects.

Clustering of optical quasars indeed is very similar to that of galaxies. The two-point correlation function in the separation range $1 - 20\,h^{-1}$ Mpc is well described by a power law, $\xi(r) = (r/r_0)^{-\gamma}$ with a slope of $\gamma = 1.9$ and a correlation length of $r_0 = 5.5\,h^{-1}$ Mpc (Ross et al. 2009; Shen et al. 2009). Further, using SDSS and 2QZ quasar sample, Croom et al. (2005) and Ross et al. (2009) track the evolution of the optical quasar clustering amplitude over the redshift range $z = 0.5 - 2.5$ and find only a mild evolution. The most recent direct measurements of the X-ray AGN clustering were presented in Gilli et al. (2005, 2009). Hickox et al. (2009) studied clustering properties of different types of AGNs at $z \approx 0.5$ through cross-correlation with the galaxy catalog. Generally, the two-point correlation function of the X-ray AGNs was found to be similar to that of the optical quasars; however, the previous X-ray studies could not constrain the evolution of the correlation function over a sufficiently wide redshift range.

The main conclusion from previous clustering analyses is that AGNs are located in galaxy group-sized dark matter halos ($M \sim 2\times10^{12}\,h^{-1}\,M_\odot$, see Ross et al. 2009), with the mass scale fairly independent of the object redshift or observed luminosity. Hickox et al. (2009) also find some differences in the clustering properties and color of host galaxies for the X-ray, radio, and infrared-selected AGNs at $z = 0.5$. The difference in the AGN clustering properties and colors of their host galaxies lead Hickox et al. to conclude that these different techniques select distinct source populations and not simply different stages of rapidly changing AGN properties.

In addition to determining the mass scale of the the AGN host dark matter halos, it is interesting to establish *where* within the halos the active galaxies are located. This question can be addressed by direct observations of individual objects only in rich galaxy clusters. Indeed, some studies (Cappi et al. 2001; Molnar et al. 2002; Martini et al. 2006) indicate an excess of X-ray AGNs in the cluster outskirts (see, however, Koulouridis & Plionis 2010). However, the majority of quasars and AGNs are located within galaxy group-sized objects, where it is hard or impossible to independently localize the centroid of the system, especially at high redshifts.

[1] Dipartimento di Astronomia, Università di Padova,Vicolo dell'Osservatorio 2, 35122 Padova, Italy
[2] Harvard-Smithsonian Center for Astrophysics, 60 Garden Street, Cambridge, MA 02138
[3] Department of Astrophysical Sciences, Princeton University, NJ 08544
[4] Hubble Fellow
[5] Carnegie-Princeton Fellow
[6] Department of Physics, Durham University, South Road, Durham, DH1 3LE, United Kingdom
[7] STFC Postdoctoral Fellow
[8] Dept. of Astronomy, The Ohio State University
[9] Dept. of Astronomy and Astrophysics, Kavli Institute for Cosmological Physics, E.Fermi Institute, The University of Chicago, Chicago, IL 60637
[10] John Hopkins University
[11] Space Research Institute (IKI), Profsoyuznaya 84/32, Moscow, Russia

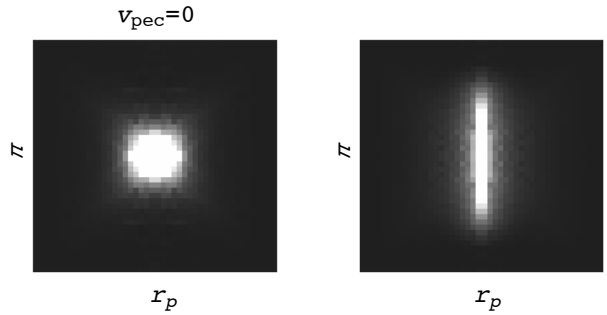

FIG. 1.— The two-dimensional correlation function $\xi(r_p, \pi)$ for objects located within dark matter halos with the maximum circular velocity $V_{max} > 250$ km s^{-1} at $z = 1$, plotted as a function of transverse (r_p) and line-of-sight (π) pair separation. 70% of objects are forced to be at the centers of such halos, while 30% are put in one of the satellite subhalos. In the left panel, the peculiar velocities were set to 0.

For such systems, it is possible to determine the fraction of objects in the satellite galaxies through analysis of the two-point correlation function at small separations. An example of such an approach can be found in Padmanabhan et al. (2009). Based on cross-correlation of the SDSS quasar and Large Red Galaxies samples, these authors argue that a high fraction, $> 25\%$, of the optical quasars must be located in non-central galaxies.

One of the main goals of the present work is to constrain the location of X-ray emitting AGNs within their host dark matter halos by a more direct method. The effect we are using is a strong dependence of a galaxy's peculiar velocity on its location within the host halo. The central galaxies are predicted (and observed, at least in massive clusters, see Oegerle & Hill 2001) to be nearly at rest with respect to the host halo, and their random motions correspond to motions of the halos as a whole. The satellite galaxies move at approximately the virial velocities *within* the halo. As a result, the satellite galaxies have much faster peculiar motions and form "finger of God" structures in the radial velocity space. The effect of high peculiar velocities of the satellite galaxies can be detected though comparison of the objects' clustering properties as a function of projected separation, r_p, and the line-of-sight separation, π. Peculiar motions do not affect r_p but can strongly distort π because it is derived from the measured redshift.

Using peculiar motions in the previous studies of the AGN clustering was hard because of the small number of objects and insufficient accuracy of the redshift measurements[12]. Fortunately, we now can use an excellent sample for such studies. The *Chandra* survey of 9.3 deg^2 in the Boötes region (Murray et al. 2005) provides a uniformly selected sample of > 3000 X-ray selected AGNs, for a uniform subsample of which (~ 1900 sources) high-quality spectra were measured with MMT/Hectospec (Kochanek et al., in preparation).

Full information on the object clustering and peculiar velocities is contained in the two-dimensional correlation function, $\xi(r_p, \pi)$. An example derived from the numerical simulations we use in this Paper is shown in Fig. 1. See, e.g., Zehavi et al. (2002) for an example of the detailed modeling of the $\xi(r_p, \pi)$ function measured for the SDSS galaxies. Unfortunately, such a detailed modeling is impossible for the present high-z AGN samples due to limited statistics. However, we show that useful information can still be obtained using projections of $\xi(r_p, \pi)$ on the radial velocity direction and on the sky plane, $\xi(\pi)$ and $\xi(r_p)$, respectively (formally defined in § 3.1 below). Using numerical cosmological simulations, we show that if a substantial fraction of objects is in satellite galaxies, $\xi(\pi)$ is expected to be significantly in excess of $\xi(r_p)$ in the range of comoving distances $1 - 10\,h^{-1}$ Mpc (§ 4.3). The observed correlation functions do not show such an excess (§ 5.1), which we exploit to put an upper limit on the fraction of X-ray AGNs in the satellite galaxies. Finally, we explore the redshift evolution of the clustering length and compute the typical mass scale of the AGN host dark matter halos and put constraints on the AGN duty cycle.

[12] For example, the redshift uncertainties corresponded to peculiar velocities of $\approx 420 - 500$ km s^{-1} in the 2QZ sample (Croom et al. 2005). Because such a high level of uncertainties, Croom et al. could not extract useful information from the velocity-space distrortions although they were included in the modeling of the spatial correlation function.

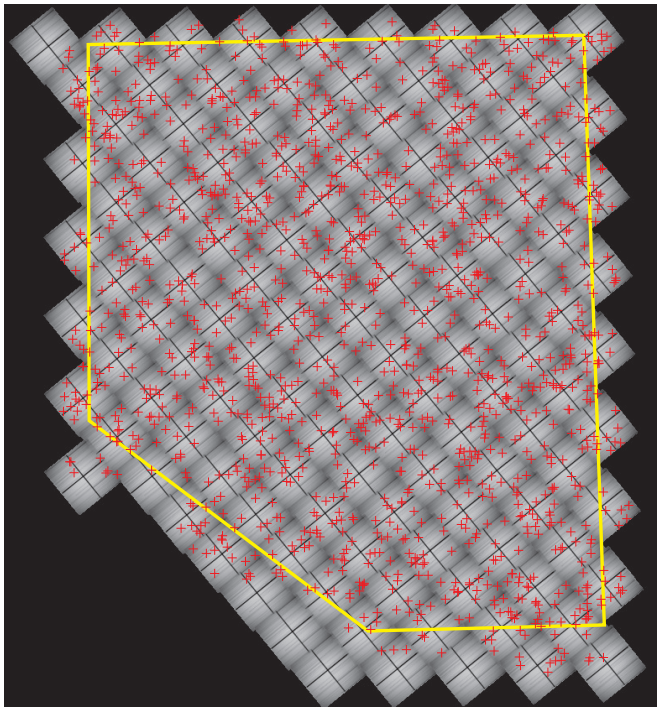

FIG. 2.— *Chandra* survey in the Boötes field. Grey scale map shows the combined *Chandra* sensitivity map (exposure maps for 126 individual pointings, each multiplied by the point source detection sensitivity as a function of off-axis distance derived in § 2.1). Crosses mark the location of X-ray sources used in this work. The polygon shows conservative boundaries of the spectroscopic survey. We consider only 1282 sources within the polygon boundaries in the clustering analysis.

All cosmology-dependent quantities are computed assuming a spatially flat model with parameters $\Omega_M = 0.268$ and $\Omega_\Lambda = 0.732$ (best-fit ΛCDM paramaters obtained from the combination of CMB, supernovae, BAO, and galaxy cluster data, see Vikhlinin et al. 2009). All distances are comoving. The parameter uncertainties are quoted at a confidence level of 68%.

2. AGN SAMPLE

We use a sample of high-z AGNs derived from the *Chandra* X-ray survey in the 9.3 deg^2 Bootes field of the NOAO Deep Wide-Field Survey (Murray et al. 2005). The region was uniformly covered with a grid of overlapping 5 ksec ACIS-I pointings providing a sensitivity of 4.7×10^{-15} erg s^{-1} cm^{-2} in the 0.5–2 keV energy band (Kenter et al. 2005). Extensive optical data exist for this field and 98% of X-ray sources have optical or infrared counterparts (Brand et al. 2006). The redshifts for X-ray sources with optical counterparts brighter than

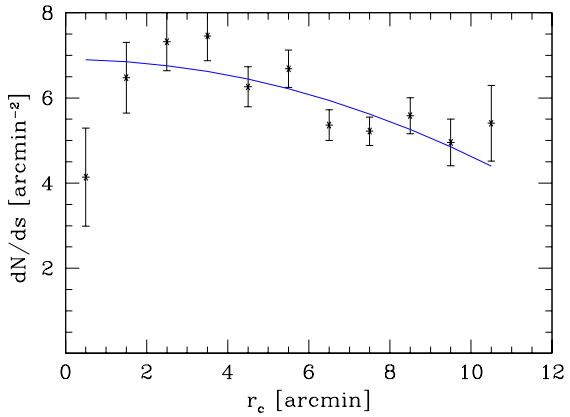

FIG. 3.— The observed surface density of detected X-ray sources as a function of the distance from the telescope optical axis. The sharp decrease at $r_c < 1'$ is attributed to the gap between the *Chandra* ACIS-I CCDs. The gradual decline at larger radii reflects the sensitivity variation caused by mirror vignetting and PSF degradation. The solid line is the best-fit second-order polynomial (eq. [1]).

$I = 21.5$ were uniformly obtained with the MMT/Hectospec instrument in the AGN and Galaxy Evolution Survey (AGES, C. S. Kochanek et al., in preparation). Further details on the X-ray and optical observations can be found in Hickox et al. (2009).

For clustering analysis, we use 1282 X-ray selected AGNs with spectroscopic redshifts. Redshift measurements effectively introduce an additional selection criterion of the sample, based on the optical magnitude of the counterparts, $I < 21.5$. This selection removes $\sim 35\%$ of the X-ray sources and likely introduces a high-z cutoff in the redshift distribution of our sources (§ 2.2). Fortunately, the redshift measurements were done with Hectospec (Fabricant et al. 2005) in several passes, which excludes the problem with the so called "fiber collisions". The locations of X-ray sources with spectroscopic redshifts are marked in Fig. 2.

To reconstruct the correlation function of sources, we need to simulate catalogs of randomly distributed sources whose distribution follows the sensitivity variations and the redshift distribution of our catalog. Below, we describe how these functions were derived from our *Chandra* sample.

2.1. *Spatial variations of sensitivity*

Chandra sensitivity for the detection of point X-ray sources is not uniform across the field of view. Sensitivity variations ($\sim \pm 25\%$, see below) are imprinted on the distribution of detected sources. The typical spatial scale of the sensitivity variations is several arcmin, which corresponds to the comoving distance of $1 - 2\,h^{-1}$ Mpc at $z = 1$. This is comparable to the distance scale where we measure clustering, therefore these variations must be taken into account.

The sensitivity variations are caused mainly by two effects — 1) the vignetting of the *Chandra* X-ray telescopes, and 2) the degradation of the Point Spread Function (PSF) away from the optical axis. The mirror vignetting is well-calibrated and its effect can be computed for a given source population. However, the effects of PSF degradation on the source detection efficiency in the low-photon regime are very complex. Therefore, it is best to measure the combined effect of the sensitivity variations empirically.

Both the mirror vignetting and PSF degradation are approximately azimuthally symmetric. Therefore, we can assume that the detection sensitivity is a function of the source offaxis angle, r_c and measure it from the radial profile of the surface density distribution of detected X-ray sources, averaged over all the 126 fields. The results is shown in Fig. 3. For a uniform sensitivity, we would expect a constant surface density, while in reality we find that the average surface density is ~ 7 arcmin^{-2} near the optical axis, and falls to ~ 5 arcmin^{-2} at off-axis distances of 10 arcmin. The derived radial profile of the source surface density can be modeled with a second-order polynomial,

$$\frac{dN}{ds} = 6.9\left(1 - (r_c/17.4')^2\right). \quad (1)$$

In addition to this gradual variation with radius, there are sharp features in the spatial sensitivity pattern related to the gaps between the *ACIS-I* CCDs. In particular, these gaps are responsible for the drop in the number of detected sources at $r_c < 1'$ in Fig. 3. These sensitivity variations can be adequately taken into account using the standard *Chandra* exposure maps.

Our final sensitivity map (Fig. 2) consists of the merged set of *Chandra* exposure maps computed for the individual 126 pointings, each multiplied by the radial sensitivity pattern given by eq. (1). This sensitivity map is taken into account in the derivation of the correlation function through the generation of the appropriate catalogs of random sources. The total area within the conservative boundaries of the spectroscopically surveyed region of the Bootes field is 7.30 deg^2. The total effective area, taking into account the gaps between the *Chandra* CCDs and degradation of the detection efficiency, is 5.90 deg^2.

2.2. *Redshift distribution*

The model for the source redshift distribution, dN/dz, should reflect both the intrinsic variations of the comoving number density with redshift and all selection effects of the catalog. A commonly used approach is to model the observed dN/dz distribution with a high-order polynomial (see, e.g., Croom et al. 2005; Ross et al. 2009, for recent examples). This approach works well for catalogs with a large number of sources. However, for smaller catalogs, like ours, there is a danger that a high-order polynomial fit will follow statistical fluctuations in the observed dN/dz, while a low-order polynomial would be unable to adequately model the strong gradients at low z. Therefore, we fit the redshift distribution of AGNs in the Bootes field with a parametric model based on several physical assumptions.

The first component of the model represents the cosmological comoving volume per unit redshift, $dN_1/dz \propto dV/dz \propto D_c^2$, where $D_c(z)$ is the comoving distance to redshift z. The second component is a power law function of the minimum luminosity which corresponds to the *Chandra* flux limit at redshift z, $dN_2/dz \propto L_{\rm min}^{\alpha/2} \propto d_L^{\alpha}$, where d_L is the luminosity distance, $d_L = D_c(1+z)$. This component represents the effect of the low-L cutoff of the intrinsic luminosity function introduced by the selection which is primarily based on *Chandra* detections. It also can describe the evolution of the luminosity function at high z. The third component is a high-z cutoff modeled by a broad Gaussian, $dN_3/dz \propto \exp\left(-d_L^2/C^2\right)$. This component can represent the high-L_x cutoff or steepening of the intrinsic AGN luminosity function, and also can describe various observational limits implicitly built into our catalog (e.g., a lower efficiency of optical identifications and redshift measurements for the highest-z X-ray sources). This simple

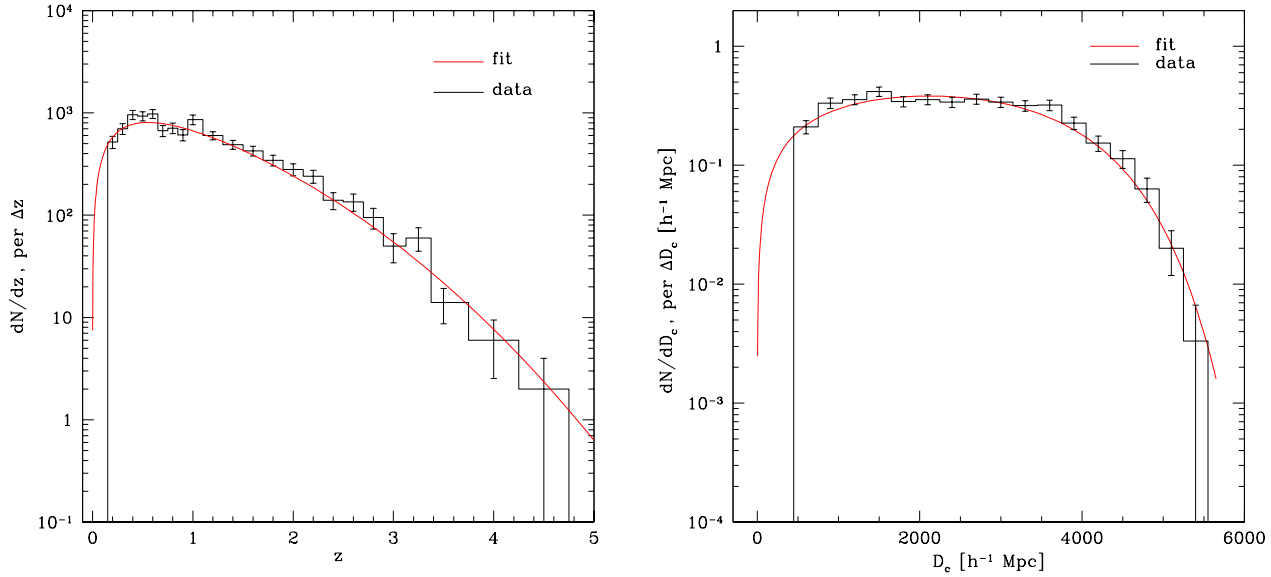

FIG. 4.— The observed distribution of *Chandra*/Boötes AGNs as a function of redshift *(left)* and comoving distance *(right)*. The lines show the analytic fit by eq. [2].

analytic model,

$$\frac{dN}{dz} = \text{const} \times \frac{dV}{dz}\, d_L^{\alpha}\, \exp\left(-(d_L/C)^2\right), \qquad (2)$$

which has only two free parameters provides a strikingly good fit to the observed redshift distribution of the Bootes X-ray selected AGNs (Fig. 4). The best-fit values are $\alpha = -1.07$ and $C = 1.50{\times}10^3\, h^{-1}$ Mpc. We also tried to introduce an intrinsic number density evolution in the first component, $dN_1/dz \propto (1+z)^{\beta}\, dV/dz$, but the best-fit values of β were consistent with zero (no evolution).

Figure 4 also demonstrates the general characteristics of our sample. The peak in the observed dN/dz distribution is near $z \approx 0.6$. The median redshift of the sample is $z_{\rm med} = 1.04$. The tail in the redshift distribution extends to $z \approx 4.5$ but the fraction of AGNs with $z > 3$ is very small. Overall, the clustering properties of sources in our sample are most sensitive to the distribution of the X-ray AGN population near $z \approx 1$.

3. TWO-POINT CORRELATION FUNCTION OF *Chandra*/Boötes AGNS

3.1. *Definitions*

Because the volume is never sampled completely in astronomical surveys, the derivation of the two-point correlation function from the data uses mock catalogs of intrinsically randomly distributed objects, which faithfully reproduces all observational distortions introduced by the survey. Example of such distortions are boundaries of the survey region, gaps in the data or spatial variations of the sensitivity, variations of the selection efficiency with redshift, etc. Given the catalog of observed sources and the mock random catalog, the two-point correlation function can be estimated (Landy & Szalay 1993) as

$$\xi = \frac{N_{\rm r}(N_{\rm r}-1)}{N_{\rm d}(N_{\rm d}-1)}\frac{DD}{RR} - \frac{N_{\rm r}-1}{N_{\rm d}}\frac{DR}{RR} + 1, \qquad (3)$$

where DD is the number of source pairs in the data for the given distance interval, RR is the corresponding number of pairs in the random catalog, DR is the number of pairs between the data and random catalog, and N_d and N_r are the numbers of objects in the data and random catalogs, respectively. Statistical uncertainties for ξ can be estimated as

$$\delta\xi = \frac{1+\xi}{\sqrt{DD}} \qquad (4)$$

(Peebles 1973); this equation includes both the Poissonian shot noise and intrinsic variance terms. We prefer to use this analytic approximation instead of jackknife sampling because our sample has a small number of objects and the jackknife estimates are too uncertain.

The correlation function in real space is expected to be isotropic, so ξ is a function of the 3D separation only. When the object redshifts are used to derive the distances, the correlation function is distorted in the line-of-sight direction because of large-scale flows (the Kaiser 1987 effect) and "fingers of God" arising within the virialized dark matter halos. The correlation function should then be measured as a function of the projected separation, π, and the line-of-sight separation, r_p. Equations [3] and [4] still can be used, but the pairs must be counted for each combination (r_p, π).

Given the angular separation between two objects, θ, and redshifts, z_1 and z_2, the comoving separations r_p and π can be computed as follows. First, one computes the radial comoving distances, $D_{c,1}$ and $D_{c,2}$, corresponding to the object redshifts (see, e.g., Hogg 1999). Then, following Davis & Peebles (1983) we have

$$\pi = |D_{c,1} - D_{c,2}|, \qquad (5)$$

and

$$r_p = \left[2D_{c,1}D_{c,2}(1-\cos\theta)\right]^{1/2}. \qquad (6)$$

One can also define a formal 3D separation,

$$s = \left(r_p^2 + \pi^2\right)^{1/2}, \qquad (7)$$

but it should be kept in mind that s is not equivalent to the true 3D separation, d, because of the redshift space distortions.

As only the line-of-sight separations, π, are affected by the object peculiar velocities, it is useful to consider the correla-

tion function projected on the sky plane,

$$w(r_p) = \int_{-\infty}^{\infty} \xi\left(\sqrt{r_p^2 + \pi^2}\right) d\pi, \quad (8)$$

because it is not modified by the redshift-space distortions (Davis & Peebles 1983):

$$\int_{-\infty}^{\infty} \xi^{(\mathrm{true})}\left(\sqrt{r_p^2 + \pi^2}\right) d\pi = \int_{-\infty}^{\infty} \xi^{(\mathrm{obs})}(r_p, \pi)\, d\pi. \quad (9)$$

Large separations do not contribute significantly to the integrals in equations 8 and 9 but add noise, therefore the integration is truncated at some line-of-sight separation. A good choice for studies of AGN sample is to truncate the integration at $\pm 40\, h^{-1}$ Mpc (see, e.g., Gilli et al. 2009).

Because of the insensitivity of $w(r_p)$ to the redshift-space distortions, most of the studies which involve detailed modeling of the shape of the galaxy two-point correlation function are based on fitting the $w(r_p)$ measurements (e.g., Zehavi et al. 2005; Padmanabhan et al. 2009). Using $w(r_p)$ instead of $\xi(r)$ is particularly straightforward in those cases when $\xi(r)$ can be sufficiently accurately approximated by a power law, $\xi(r) = (r/r_0)^{-\gamma}$. It follows from eq. [8] that in this case the relation between ξ and $w(r_p)$ is simply (Peebles 1980)

$$w(r_p) = A(\gamma)\, r_p\, (r_p/r_0)^{-\gamma}, \quad (10)$$

where

$$A(\gamma) = \Gamma(1/2)\Gamma[(\gamma - 1)/2]/\Gamma(\gamma/2). \quad (11)$$

Therefore, the correlation length, r_0, and the slope of the true 3D correlation function ξ can be obtained immediately from the power-law fit to $w(r_p)$.

In this work, we also consider a projection of the measured 3D correlation function on the line-of-sight direction,

$$w(\pi) = \int_{-\infty}^{\infty} \xi^{(\mathrm{obs})}(r_p, \pi)\, dr_p. \quad (12)$$

In the absence of peculiar motions, $w(\pi)$ should be equivalent to $w(r_p)$. In particular, for a power-law $\xi(d)$, eq. [10] will be valid also for $w(\pi)$.

In practice, the integration in eq. 12 and 8 is truncated at comoving separations $\pm 40\, h^{-1}$ Mpc to minimize noise. Assuming that the true correlation function follows a power law with index γ at large separations, we can calculate the effect of this truncation as

$$C_\gamma(r) = \frac{\int_0^{40} \left(r^2 + l^2\right)^{-\gamma/2}\, dl}{\int_0^{\infty} \left(r^2 + l^2\right)^{-\gamma/2}\, dl}. \quad (13)$$

The correction coefficient, $C_\gamma(r)$, is close to 1 for $r \ll 40\, h^{-1}$ Mpc and gradually decreases at larger distances. For $\gamma = 2$ (close to our best-fit value), $C_\gamma = 0.94$ at $r = 2\, h^{-1}$ Mpc, 0.86 at $r = 6\, h^{-1}$ Mpc ($\approx$ the correlation length), and 0.65 at $r = 20\, h^{-1}$ Mpc ($\approx$ the largest separation at which the projected correlation is still marginally detectable).

Using equations 10 and 13, we can define the quantities

$$\xi(r_p) \equiv \frac{1}{A(\gamma)\, C_\gamma(r_p)} \frac{w(r_p)}{r_p} \quad (14)$$

and

$$\xi(\pi) \equiv \frac{1}{A(\gamma)\, C_\gamma(\pi)} \frac{w(\pi)}{\pi}, \quad (15)$$

where γ is determined from the power-law fit to the measured $w(r_p)$ (eq. [10]). Thus defined, $\xi(r_p)$ should be a close approximation to the true 3D correlation function $\xi(r)$. In the absence of redshift-space distortions, $\xi(\pi)$ also should approximate $\xi(r)$. However, the peculiar motions (and in particular, the "finger of God" effect) suppress $\xi(\pi)$ on the smallest separations and enhance it relative to $\xi(r)$ on the intermediate scales (see below). Therefore, $\xi(r_p)$ can be used to determine the correlation length of our objects and hence the mass scale of their host dark matter halos. The ratio $\xi(\pi)/\xi(r_p) = w(\pi)/w(r_p)$ reflects the amplitude of the peculiar motions and hence can be used to constrain the fraction of objects located in the satellite dark matter subhalos.

3.2. *Results*

The correlation functions $\xi(r_p)$ and ξ_π derived for our complete sample are shown in Fig. 5a (filled and open circles, respectively). Technically, we derive the functions as follows. First, we estimate the two-dimensional correlation function, $\xi(r_p, \pi)$, on a grid of separations with equal logarithmic width for each cell, $\Delta \log d = 0.2$. We use the Landy & Szalay estimator (eq. 3). The random catalog is generated using the spatial sensitivity map and the model for the redshift distribution in our sample (§ 2.1 and 2.2). To minimize the additional noise, the number of objects in the random catalog is a factor of 100 larger than that for the AGN sample. The derived $\xi(r_p, \pi)$ is then integrated in the radial and sky plane directions to obtain $w(r_p)$ and $w(\pi)$ (eq. 9 and 12). As discussed in § 3.1, the integration is limited to separations $\pm 40\, h^{-1}$ Mpc to minimize noise. We then fit a power law (eq. 10) to $w(r_p)$ to measure the slope of the correlation function, $\gamma = 1.97 \pm 0.09$. The correlation length measured for the full sample is $r_0 = 6.27 \pm 0.33\, h^{-1}$ Mpc. We then compute the renormalization factor $A(\gamma)$ (eq. 11) and correct for the truncation of the integration in $w(r_p)$ and $w(\pi)$ at $40\, h^{-1}$ Mpc (eq. 13). With the renormalization factors determined, we convert $w(r_p)$ and $w(\pi)$ into $\xi(r_p)$ and $\xi(\pi)$ using eq. [14–15].

As discussed above, $\xi(r_p)$ should be close to the true 3D correlation function $\xi(d)$, while $\xi(\pi)$ should be distorted by peculiar motions of the AGN host galaxies. Indeed, we observe a strong suppression in $\xi(\pi)$ relative to $\xi(r_p)$ at separations $\pi < 1\, h^{-1}$ Mpc. Unfortunately, the corresponding radial velocity difference, $\Delta z \approx 0.0003$, is uncomfortably close to the uncertainties in the AGES redshift measurements (Kochanek et al., in preparation). Therefore, we ignore the $\xi(\pi)$ data at $\pi < 1\, h^{-1}$ Mpc. At intermediate separations ($r \approx [1 - 10]\, h^{-1}$ Mpc), $\xi(\pi)$ is expected to be enhanced by the peculiar motions (see below). No such enhancement is present in our data. In fact, the ratio $\xi(\pi)/\xi(r_p)$ is fully consistent with 1 at separations $> 1\, h^{-1}$ Mpc within the measurement uncertainties (Fig. 5b). Below, we show that this can be used to put an upper limit on the fraction of AGNs that can reside in satellite galaxies orbiting within massive dark matter halos.

3.2.1. *Comparison with previous measurements*

Our results represent the most accurate measurement of the spatial clustering of X-ray selected AGNs to date, so a comparison with earlier observations is useful.

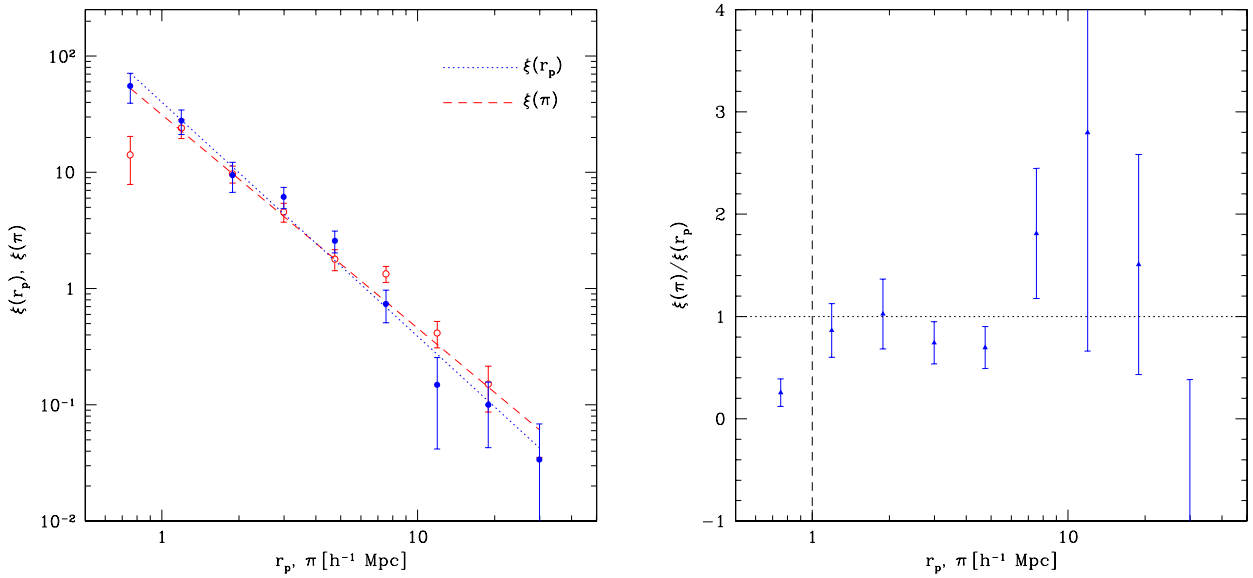

FIG. 5.— *(a)* The two-point correlation functions of Bootes/*Chandra* AGNs estimated from projections on the sky plane ($\xi(r_p)$, filled circles) and on the line of sight ($\xi(\pi)$, open circles). See § 3.2 for the description of our procedure to derive $\xi(r_p)$ and $\xi(\pi)$. *(b)* The ratio of two projected functions. At small separation ($\pi \lesssim 1\,h^{-1}$ Mpc, indicated by the vertical dashed line), the ratio can be affected by uncertainties of the AGES redshift measurements. At larger separations, we observe no statistically significant difference between $\xi(r_p)$ and $\xi(\pi)$.

The first detection of angular clustering of X-ray sources was reported by Vikhlinin & Forman (1995) based on the analysis of the *ROSAT* PSPC data. Using the Limber equation reconstruction (Peebles 1980), these authors estimated a correlation length of $19 \pm 5\,h^{-1}$ Mpc (comoving) at $z = 1.5$ using raw measurements, and $7.5 \pm 2\,h^{-1}$ Mpc after correcting for the "amplification" bias caused by the poor angular resolution of the *ROSAT* PSPC. The latter value is in good agreement with our results.

Our results also are in good agreement with direct measurements of the spatial clustering in the ROSAT NEP survey (Cappelluti et al. 2007), *Chandra* surveys in Deep Fields North and South (Gilli et al. 2005), and the *XMM-Newton* COSMOS field (Gilli et al. 2009). Correlation lengths for the X-ray AGNs have been estimated also from the Limber inversions of the angular clustering measured for the *XMM-Newton* and *Chandra* sources. A wide range of r_0 values can be found in the literature (e.g., Plionis et al. 2008, and references therein); our measurements are inconsistent with $r_0 > 10\,h^{-1}$ Mpc reported in some of these analyses.

4. AGN CLUSTERING MODEL

In the past ten years, a very successful framework for modeling the nonlinear clustering properties of galaxies has been developed (the so called Halo Occupation Distribution (HOD) model, see Seljak 2000; Ma & Fry 2000; Peacock & Smith 2000; White et al. 2001; Scoccimarro et al. 2001; Berlind & Weinberg 2002; Berlind et al. 2003, among others). The approach is based on the idea that the distribution of dark matter can be fully described through the mass function, linear bias, and density profiles of dark matter halos. These elements are well-calibrated using N-body simulations. The two additional ingredients of the model, which are less well known, are the probability distribution for a halo of mass M to contain N galaxies, and the distribution of galaxies within the halos. These functions can be parameterized by the functions suggested by the results of high-resolution numerical simulations (e.g., Kravtsov et al. 2004), and some parameters of the model can be in fact determined by fitting the observed correlation functions. In particular, Kravtsov et al. (2004) and Zheng et al. (2005) show that the elements of HOD can be effectively decomposed into two components, separately describing the properties of central and satellite galaxies within the dark matter halos.

The HOD model is now very well developed for fitting the *shape* of the two-point correlation function. This technique has been applied to modeling the projected two-point correlation functions, $w(r_p)$, for objects ranging from Lyman-break galaxies at $z = 3 - 5$ (Conroy et al. 2006) to relatively low-z quasars from SDSS (Padmanabhan et al. 2009). Recently, the HOD approach has been developed also for modeling the redshift-space distortions in the galaxy correlation functions (Tinker et al. 2006; Tinker 2007) — just the type of information we are aiming to use in this work to constrain the locations of Bootes/*Chandra* AGNs within the host dark matter halos.

In principle, the HOD models for galaxy clustering are analytic, and thus are convenient for those applications in which the cosmological parameters are varied. However, some of the most essential parameters of the HOD models are calibrated using numerical simulations. If one is interested in varying the parameters of galaxy distribution at a fixed redshift in a fixed cosmological model, it is more accurate — and easier — to obtain the model correlation functions directly from numerical simulations rather than to rely on analytic approximations derived from analyzing the simulations. This is the approach we take here.

4.1. *Numerical Simulations*

The set of simulations we use in this work is described in Tasitsiomi et al. (2004) and Conroy et al. (2006). These are high-resolution dissipationless simulations run in a flat ΛCDM cosmology with parameters close to the present-day "concordance" values, $\Omega_{\rm M} = 0.3$, $h = 0.7$, and $\sigma_8 = 0.9$. The simulations follow the evolution of dark matter in a $120\,h^{-1}$ Mpc box. The box contained 512^3 dark matter particles with mass $m_p = 1.07 \times 10^9\,h^{-1}\,M_\odot$; the peak resolution reached $1.8\,h^{-1}$ kpc.

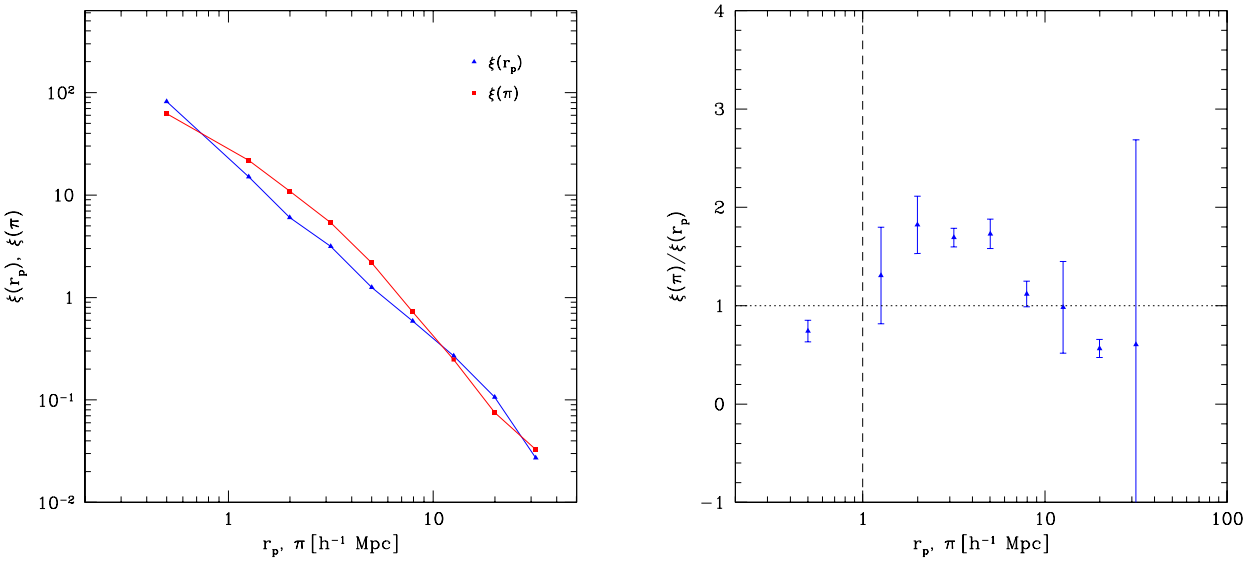

FIG. 6.— Correlation functions of all objects in the simulation output (both halos and subhalos) with $v_{\rm max} > 300\,{\rm km\ s^{-1}}$. The amplitude of the $\xi(r_p)$ function (left panel) matches the observed correlation length of the *Chandra*/Boötes sample, $r_0 = 6.27\,h^{-1}$ Mpc. However, many objects with such $v_{\rm max}$ are satellites in larger halos. This results in large peculiar motions leading to strong distortions of $\xi(\pi)$ with respect to $\xi(r_p)$. The ratio of $\xi(\pi)/\xi(r_p)$ averaged over three viewing directions of the simulation box at $z = 1$ is shown in the right panel (the uncertainties represent the scatter between the viewing directions). The predicted ration in the $2 - 6\,h^{-1}$ Mpc separation range is ≈ 1.8, inconsistent with the observed correlation functions (see Fig. 5).

The locations and velocities of the dark matter particles in the simulations were recorded at $z = 0.09$, 0.5, 1.0, 2.0, 3.1, 4.0, and 5.0, matching well the redshift distribution in the Bootes/*Chandra* AGN sample (see Fig.4). The simulation outputs were then analyzed to identify dark matter halos and subhalos using a modification of the Klypin et al. (1999) bound density maxima halo-finding algorithm (see Kravtsov et al. 2004, for details). The main steps of this procedure are identification of local density peaks, and analysis of the density, circular velocity, and velocity dispersion profiles with simultaneous removal of unbound particles. The final profiles, using only bound particles, are used to calculate the halo properties such as the circular velocity profile $V_{\rm circ} = [GM(< r)/r]^{1/2}$ and the maximum circular velocity, $v_{\rm max}$. The completeness limit for halo identification using this procedure is ~ 50 particles. The corresponding $v_{\rm max}$ limit is $\sim 80\,{\rm km\ s^{-1}}$, and the associated mass limit is $\sim 5 \times 10^{10}\,M_\odot$. The best-fit power law to the $v_{\rm max} - M_{180}$ relation[13] derived in these simulations at $z = 1$ is

$$\log M_{180} = 4.57 + 3.21\ \log v_{\rm max}. \qquad (16)$$

The identified halos were then classified into host halos whose centers are not located within any larger virialized systems, and subhalos which lie within the virial radius of a larger system (see Tasitsiomi et al. 2004, for details of this procedure). Briefly, a halo is classified as a subhalo if its center is within r_{180} of the center of a more massive halo, where r_{180} is the radius which corresponds to a mean spherical overdensity of 180 relative to the mean density at the given redshift. In the real Universe, centers of host halos can be identified as locations of the groups' central galaxies, while subhalos correspond to satellite galaxies.

4.2. *Model of the AGN population*

[13] Hereafter, we use the mass defined within an overdensity threshold of 180 with respect to the mean density of the Universe at the given redshift. The correspondence between $v_{\rm max}$ and mass is quoted for $z = 1$ unless the redshift is stated explicitly.

Our data can constrain the following two basic properties of the AGN population. First, the overall clustering amplitude observed in $\xi(r_p)$ constrains the mass scale of the AGN host dark mtter halos. Note that it is the mass scale of host halos, not of individual subhalos in which the AGNs might reside, which is constrained by the $\xi(r_p)$ amplitude. For example, a population of small subhalos with $v_{\rm max} = 50\,{\rm km\ s^{-1}}$ which are located within larger halos with $v_{\rm max} = 300\,h^{-1}\,{\rm km\ s^{-1}}$ has the clustering length which closely matches that for big host halos, and not that for the entire population of $v_{\rm max} = 50\,{\rm km\ s^{-1}}$ halos. Therefore, the first parameter of the model we use to characterize the spatial distribution of AGNs is the minimum $v_{\rm max}$ for the halos which can contain the X-ray AGNs. The AGN can be located either at the center of such a halo or in any of its smaller subhalos.

Note that we choose to characterize the halos using their $v_{\rm max}$ rather than the virial mass for the reasons outlined in Kravtsov & Klypin (1999), Nagai & Kravtsov (2005), and Conroy et al. (2006). The maximum circular velocity is a more direct measure of the depth of the halo potential wells. It reflects the central properties of the halo better, and is less subject to the effects of tidal stripping, than the halo virial mass which is dominated by the matter at large radii. Therefore, we can expect that the stellar content of the halo and all baryonic processes in the center, including the AGN activity, are better correlated with $v_{\rm max}$ than with $M_{\rm vir}$. Nagai & Kravtsov (2005) and Conroy et al. (2006) argue further that the best indicator for the stellar mass of *subhalos* is their $v_{\rm max}$ before accretion onto the host halo. Since our results are not very sensitive to the $v_{\rm max}$ threshold for subhalos (see below), we do not make this distinction.

For a fixed threshold of the host halo $v_{\rm max}$, the correlation length of astronomical objects only weakly depends on whether these objects are located in the halo central galaxies or in smaller subhalos. As discussed above, the ratio $\xi(\pi)/\xi(r_p)$ should be a much more sensitive and direct indicator for the satellite fraction. We parameterize this fraction by the probability, f, for objects to reside in the central galax-

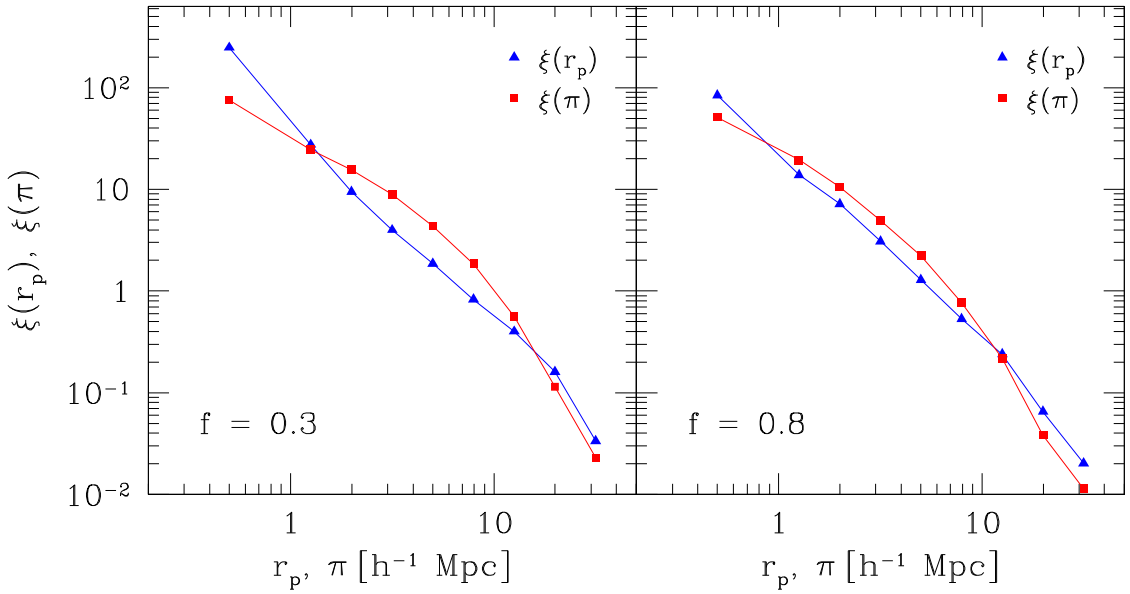

FIG. 7.— The projected correlation functions for halo samples at $z = 1$ with $v_{\rm max} > 250$ km s^{-1}, calculated with $f = 0.3$ and $f = 0.8$. The correlation functions for smaller f (more AGNs in the satellite galaxies) show a stronger "1-halo" term at small separations [$\xi(r_p)$] and a stronger presence of the "finger of God" effect [$\xi(\pi)$].

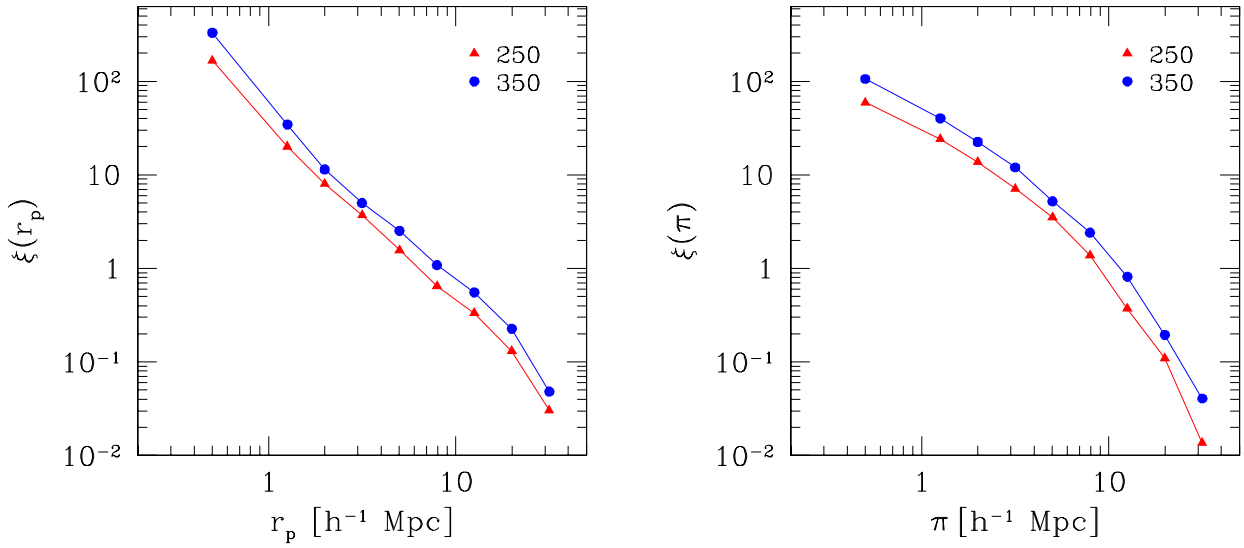

FIG. 8.— The projected correlation functions of halo samples at $z = 1$, calculated for $V_{\rm min} = 250$ and 350 km s^{-1} and $f = 0.5$. The trend with $V_{\rm min}$ is mainly equivalent to a uniform scaling of the correlation amplitude at all separations.

ies of host halos; $1 - f$ is, therefore, the probability for objects to reside in any of the smaller subhalos. The two parameters, the $v_{\rm max}$ threshold, $V_{\rm min}$, and the probability f, fully specify the relation between our model AGN population and the dark matter halos and subhalos identified in the numerical simulations. $V_{\rm min}$ is primarily constrained by the correlation length of $\xi(r_p)$, and f is mostly constrained by the $\xi(\pi)/\xi(r_p)$ ratio.

Algorithmically, we simulate the AGN locations by randomly drawing the halos and subhalos from the simulation box according to the parameters $V_{\rm min}$ and f. First, we select all bound structures (both halos and subhalos) with $v_{\rm max} > 80$ km s^{-1}. This threshold is slightly higher than the resolution limit in the simulations. We verified that the final results are nearly the same when this initial threshold is varied between 50 km s^{-1} and 100 km s^{-1}. We then select only those subhalos which are contained within halos with $v_{\rm max}$ above the given value of $V_{\rm min}$. We then randomly put a small number of objects (10–100) within the simulation box[14]. With the probability $1 - f$, the object is associated with one of the selected subhalos, and with the probability f it is put in the center of one of the halos. This procedure is repeated multiple times randomly selecting one of the box axes as the line of sight. Using these simulated objects, we derive a model of $\xi(r_p)$ and $\xi(\pi)$ for each combination of $V_{\rm min}$ and f.

If we attempt to populate the halos in these simulations with AGNs without making a distinction of main halos and subhalos, we obtain a model correlation functions which are inconsistent with the data. For example, we can adjust the

[14] This is done to approximate the low space density of *Chandra*/Boötes AGNS.

amplitude of the model correlation function by changing the $v_{\rm max}$ threshold for the halo to be able to host an AGN. The observed correlation length, $r_0 = 6.27\,h^{-1}$ Mpc, is matched if we consider all objects with $V_{\rm min} > 300\,{\rm km\ s^{-1}}$. However, the population of such halos and subhalos in the simulations shows significant redshift-space distortions (Fig. 6). In particular, the ratio $\xi(\pi)/\xi(r_p)$ is ≈ 1.8 in the range of separations $2-6\,h^{-1}$ Mpc, which is clearly inconsistent with observations (Fig. 5). Therefore, application of our more complicated model to distinguish the locations of central and satellite galaxies, is warranted.

4.3. *Model Correlation Functions $\xi(r_p)$ and $\xi(\pi)$*

The correlation functions $\xi(r_p)$ and $\xi(\pi)$ were derived from the simulation outputs on a grid of parameters within the range $V_{\rm min} \in [200; 370]\,{\rm km\ s^{-1}}$ and $f \in [0; 1]$. Examples are shown in Fig. 7 and 8. Comparison of the two panels in Fig. 7 illustrates the effect of f on the correlation functions. For smaller f (more objects located in satellite galaxies, left panel), the projected correlation function $\xi(r_p)$ shows a stronger component at $d < 1\,h^{-1}$ Mpc in excess of a power law extrapolation from larger separations. This excess is attributed to the "1-halo" term in the analytic halo model of the correlation function. At the same time, $\xi(\pi)$ shows a larger suppression of the correlation amplitude at $d < 1\,h^{-1}$ Mpc with respect to $\xi(r_p)$ at the same separations, and a stronger enhancement over $\xi(r_p)$ at $d = 2-10\,h^{-1}$ Mpc for small f. This is the consequence of a stronger "finger of God" effect in the case when more objects are located in the satellite galaxies. Unfortunately, the statistical uncertainties in the real data do not allow a detailed modeling of the observed $\xi(r_p)$ at small separations. Modeling of the $\xi(\pi)$ at small separations is further complicated by the effect of uncertainties in the redshift measurements (§ 3.2). At large separations, $\gtrsim 0.1$ of the simulation box size, the correlation functions derived from the simulations are not reliable (Kravtsov et al. 2004; Colín et al. 2006; Conroy et al. 2006). Taking all these considerations into account, we will match the observed and model correlation functions in the intermediate range of radii, $d = 1-12\,h^{-1}$ Mpc.

First, we compute the correlation length, r_0, for each combination $(V_{\rm min}, f)$. This is done by fitting a power law function, $(r_p/r_0)^{-\gamma}$, to $\xi(r_p)$ in the range $r_p = 1-12\,h^{-1}$ Mpc. We then compute the ratio $\xi(\pi)/\xi(r_p)$ (an example is shown in Fig. 9) and fit it in the same range of separations with a modified log-normal function,

$$\phi(d) = 1 + A\exp\left(-\left[\frac{(\log d - \log d_0)^2}{2D^2}\right]^g\right). \qquad (17)$$

The index g is fixed at the mean best-fit value for all $(V_{\rm min}, f)$ combinations, $g = 1.2$. The $\xi(\pi)/\xi(r_p)$ ratio derived from the simulations shows substantial variations related to cosmic variance (this can be estimated by comparing the results for three viewing angles, see errorbars in Fig. 9). Therefore, we need to smooth the results of fit by eq. 17. This is achieved by fitting low-order polynomials to the parameters D, d_0, and A as a function of $V_{\rm min}$ and f. We found that the adequate description is achieved if the best-fit values of D and d_0 are approximated as a linear function of f, and $A(V_{\rm min}, f)$ is fit by a second-order polynomial. An example of the fitting function derived from this smooth map is shown in Fig. 9.

4.4. *Application to the Data*

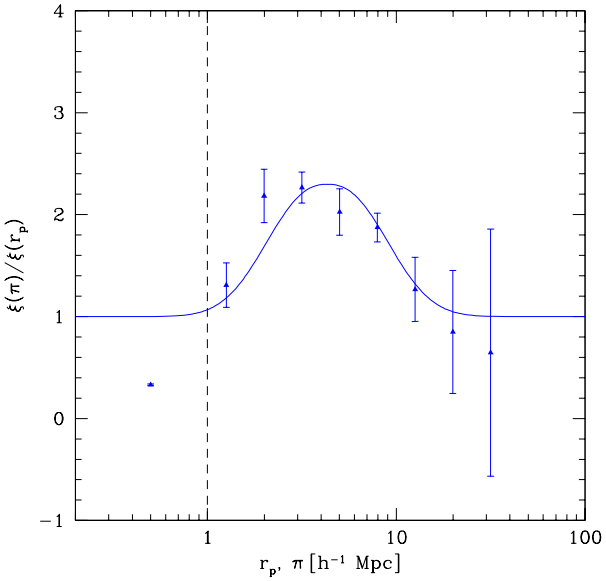

FIG. 9.— The ratio of the model correlation functions computed for $f = 0.5$ and $V_{\rm min} = 310\,{\rm km\ s^{-1}}$. Uncertainties at each separation are estimated using the variance of the ratio computed for 3 different viewing angles and reflect mostly the cosmic variance. The solid line shows the analytic approximation (eq. 17).

In applying the correlation function model to the data we avoid including any sensitivity to the *slope* of the correlation function. The primary motivation is that the best-fit slope to the correlation functions derived from numerical simulations is slightly different from our best-fit value — the average power law slope of the model $\xi(r_p)$ functions is in the range $\gamma = 1.6-2.0$ for $d < 20\,h^{-1}$ Mpc separations vs. our best-fit value of 1.97 ± 0.09 (§ 3.2). This may indicate that our method of assigning the AGN locations to the dark matter halos is overly simplistic. Alternatively, this disagreement may arise because a combination of the cosmological parameters used in the simulation is slightly different from the currently accepted values, resulting in a possible mismatch between the slopes of the model and the real correlation function of astronomical objects. The most relevant combination of parameters is the product $\Omega_M h$. The most recent results from the WMAP 7-year data release (Komatsu et al. 2010) indicate $\Omega_M h = 0.19$ while in the simulations $\Omega_M h = 0.21$. Therefore, we rely on those properties of the correlation function which are less sensitive to the details of the modeling procedure and exact values of the cosmological parameters.

First, we use the value of the correlation length derived from fitting the $\xi(r_p)$ function (§ 3.2). Second, we use the ratio $x = \xi(\pi)/\xi(r_p)$ in the range of separations $1-12\,h^{-1}$ Mpc. For halos with circular velocities $v_{\rm max} \sim 300\,{\rm km\ s^{-1}}$ (as indicated by the amplitude of the AGN correlation function, see below), the "fingers of God" extend to $v_{\rm max}/H \sim 3\,h^{-1}$ Mpc, just in the middle of this range of separations. Formally, the constraints on the parameter of the AGN population model, $V_{\rm min}$ and f, are derived using a χ^2 function computed as

$$\chi^2 = \frac{(r_0 - r_0^{\rm mod})^2}{\sigma_{r0}^2} + \sum\frac{(x - x^{\rm mod})^2}{\sigma_x^2} \qquad (18)$$

where the summation in the second term is over the data points in the $1-10\,h^{-1}$ Mpc separation range, and the model functions are those described in § 4.3.

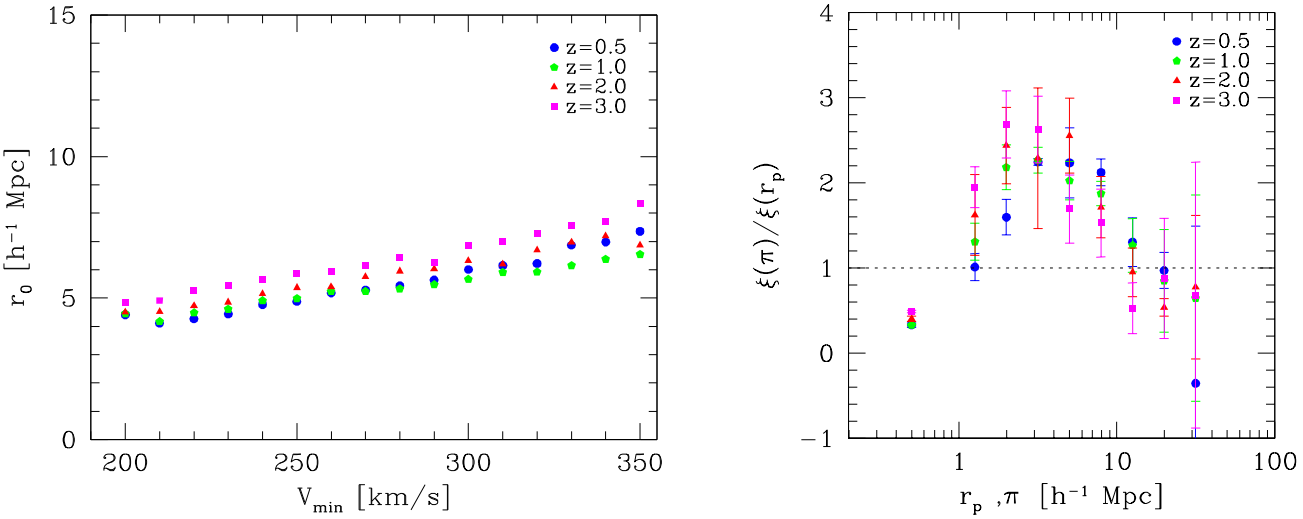

FIG. 10.— *Left:* Dependence of r_0 on $V_{\rm min}$ for the objects at the centers of distinct halos ($f = 1$) for the simulation outputs at $z = 0.5$, 1, 2, and 3. There is almost no change with redshift for $z \lesssim 2.5$. *Right:* the ratio of $\xi(\pi)/\xi(r_p)$ for the population model with $V_{\rm min} = 310\,{\rm km\ s^{-1}}$ and $f = 0.5$ (50% of objects are in the satellite galaxies of the $v_{\rm max} > 310\,{\rm km\ s^{-1}}$ halos). Any difference in this ratio between different simulation snapshots is within the uncertainties (estimated from analyzing 3 different projections for each snapshot).

TABLE 1
CLUSTERING MODELING RESULTS AS A FUNCTION OF REDSHIFT

Redshift range	$z_{\rm med}$ (2)	$\langle \log L_x \rangle$ (3)	r_0 (4)	$V_{\rm min}$ (5)	$M_{\rm lim}$ (6)	n (7)	$n_{\rm halo}$ (8)	$n/n_{\rm halo}$ (9)
0.172 – 0.555	0.374	42.58	5.40 ± 0.46	271 ± 23	3.5 ± 0.9	1.54×10^{-4}	$1.40^{+0.46}_{-0.32}$	$0.110^{+0.032}_{-0.027}$
0.555 – 1.000	0.738	43.34	5.67 ± 0.64	287 ± 33	3.4 ± 1.3	6.12×10^{-5}	$1.23^{+0.62}_{-0.38}$	$0.050^{+0.022}_{-0.017}$
1.000 – 1.630	1.279	43.85	6.96 ± 0.80	362 ± 45	5.2 ± 2.1	2.56×10^{-5}	$0.46^{+0.35}_{-0.19}$	$0.056^{+0.039}_{-0.024}$
1.630 – 5.0	2.099	44.28	6.46 ± 1.46	308 ± 70	2.1 ± 1.2	8.61×10^{-6}	$0.82^{+1.43}_{-0.50}$	$0.011^{+0.016}_{-0.007}$

NOTE. — Column (4) — best-fit correlation length assuming a fixed slope of $\gamma = 1.97$, in units of h^{-1} comoving Mpc. Column (5) — threshold maximum circular velocity of the host dark matter halos, in units of km s^{-1} (§5.2). Column (6) — the halo virial mass corresponding to $V_{\rm min}$, in units of $10^{12}\,h^{-1}\,M_\odot$. Column (7) — comoving number density of X-ray sources at $z_{\rm med}$, in units of $h^3\,{\rm Mpc}^{-3}$. Column (8) — comoving number density of dark matter halos with $v_{\rm max} > V_{\rm min}$ at $z_{\rm med}$, in units of $10^{-3}\,h^3\,{\rm Mpc}^{-3}$. Column (9) — probability for the *Chandra*/Boötes AGNs to be in active state computed as the ratio of number density of AGNs and the dark matter halos with $v_{\rm max} > V_{\rm min}$.

4.4.1. *Redshift Trends*

The procedure described above provides a correlation function model at the redshifts where the simulation outputs were saved. The *Chandra*/Boötes AGNs span a wide redshift range and we have to bin the data into several redshift intervals to achieve an acceptable level of accuracy for the correlation function measurements. Therefore, we need to account for any z-dependent trends of the correlation function models.

Fortunately, for our choice of observables, r_0 and the $\xi(\pi)/\xi(r_p)$ ratio, the redshift trends are very weak. This is illustrated in Fig. 10. The left panel shows r_0 as a function of $V_{\rm min}$ for a population model with $f = 1$ (all objects are at the centers of distinct halos) for the simulation outputs at $z = 0.5$, 1, 2, and 3. Obviously, there is almost no change in r_0 for a fixed $V_{\rm min}$ at $z < 3$. Any changes are much smaller than the uncertainties of our r_0 measurement even for the combined sample. Therefore, we conclude that the model r_0 as a function of $V_{\rm min}$ does not evolve over our redshift range of interest.[15] The ratio $\xi(\pi)/\xi(r_p)$ also shows little, if any, evolution with redshift. The right panel in Fig. 10 shows the results for the population model with $V_{\rm min} = 310\,{\rm km\ s^{-1}}$ and $f = 0.5$ (50% of objects are in the satellite subhalos of $v_{\rm max} > 310\,{\rm km\ s^{-1}}$ halos). Any difference between the simulation outputs is within the uncertainties (estimated from analyzing three different projections for each simulation output).

The lack of evolution in the clustering model over our redshift interval (and also the lack of detectable evolution of r_0 with z, see § 5.2 below) indicates that we can safely combine the data over the entire redshift range in the sample. Furthermore, there is no need to weight the models with the redshift distribution — one simply can use the results for the simulation output at $z = 1$. We take this approach in fitting the parameters of the population model, $V_{\rm min}$ and f (§ 5.1). In addition, we constrain the evolution of $V_{\rm min}$ with z (§ 5.2) under the assumption that the fraction of AGNs in the subhalos does not evolve (i.e., using a fixed f derived from the analysis of the entire sample).

4.4.2. *Adjusting the Results to a Low-σ_8 Cosmology*

Finally, we note that the numerical simulations we use were run assuming a high value of the power spectrum normalization, $\sigma_8 = 0.9$ at $z = 0$. This results in an incorrect prediction of the correlation amplitude for halos of a given mass, and thus slightly biases the derived parameters of the AGN

[15] Note that r_0 as a function of *mass* does evolve with redshift, as expected. However, this evolution appears to be canceled by the evolution in the $r_0 - v_{\rm max}$ relation and the trend of r_0 with M at a given redshift.

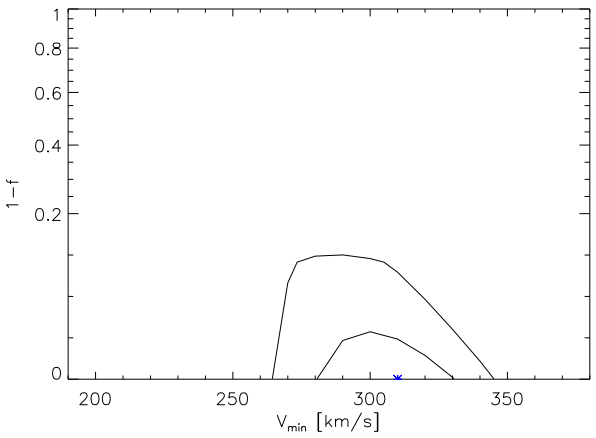

FIG. 11.— Combined constraints on halo occupation parameters, $V_{\rm min}$ and f, obtained from the full sample of the *Chandra*/Boötes AGNs. The best fit ($V_{\rm min} = 310\,{\rm km\ s^{-1}}$ and $f = 1$) is indicated with a star. The contours correspond to 68% and 95% confidence regions for two interesting parameters ($\Delta\chi^2 = 2.3$ and 6.2, respectively). The quantity $1 - f$ represents the fraction of AGNs residing in the satellite galaxies.

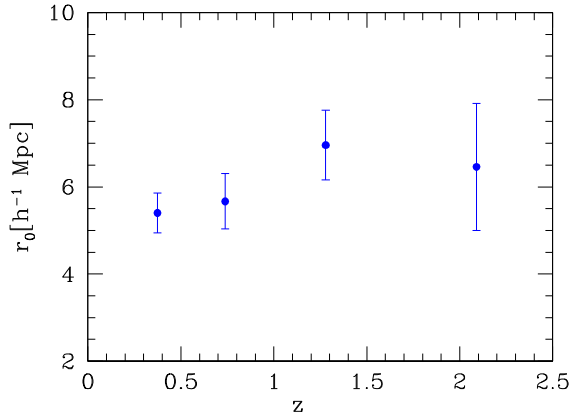

FIG. 12.— The correlation lengths, r_0, measured in 4 redshift intervals, z = [0.172 – 0.555], [0.555 – 1.000], [1.000 – 1.630], and [1.630 – 5.0], containing 320, 307, 344, and 311 objects, respectively. The values of r_0 were obtained by fitting the projected correlation function, $w(r_p)$, in each bin assuming the fixed slope of the correlation function $\gamma = 1.97$ (the best-fit value for the entire sample).

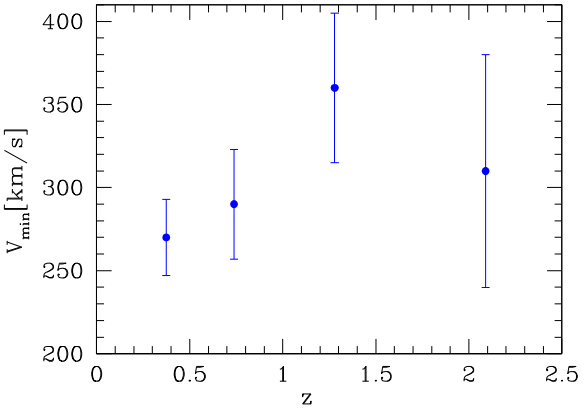

FIG. 13.— Minimum rotational velocity for dark matter halos, corresponding to the correlation lengths in Fig. 12.

population model, in particular, $V_{\rm min}$. Obviously, it would be best to use the simulations performed for the currently favored cosmological model with $\sigma_8 \approx 0.8$ but in general, these were unavailable at the time of this investigation. In Appendix A, we describe a procedure which can be used to scale the results from the comparison with the simulation to any desired cosmology. In particular, if we use the best-fit flat ΛCDM cosmological model derived from the joint analysis of the galaxy cluster mass function and other cosmological datasets, $\sigma_8 = 0.786$ and $\Omega_M = 0.268$ (Vikhlinin et al. 2009), the masses reported below should be scaled by a factor of 0.69, the $V_{\rm min}$'s decreased by 10%, and the number density of objects increased by 20%.

5. MODELING RESULTS

5.1. $V_{\rm min}$ *and the Satellite Fraction for the Entire Sample*

Figure 11 shows the combined constraints on the population model parameters, $V_{\rm min}$ and f, obtained from fitting the full sample of *Chandra*/Boötes AGNs. The best-fit velocity threshold is $V_{\rm min} = 310 \pm 13\,{\rm km\ s^{-1}}$ (68% CL one-parameter uncertainty). At $z = 1$, this corresponds to $M_{180} = 3.7\times10^{12}\,h^{-1}\,M_\odot$, or $2.2\times10^{12}\,h^{-1}\,M_\odot$ after correcting for the lower-σ_8 cosmology (see § 4.4.2 and Appendix A)[16]. We thus conclude, in agreement with the earlier studies (Gilli et al. 2009; Hickox et al. 2009), that the X-ray AGNs at high redshifts reside in small galaxy groups with masses of a factor of a few above the present-day mass of the Milky Way.

As expected from the striking agreement of the observed $\xi(r_p)$ and $\xi(\pi)$ projected correlation function, the best fit is $f = 1$, i.e. *all AGNs are located at the centers of distinct dark matter halos*. The 95% CL upper limit on the satellite fraction is $1 - f < 0.09$. This limit is lower than the 11% fraction of $v_{\rm max} > 310\,{\rm km\ s^{-1}}$ objects located within bigger halos in the simulation. We thus find that the X-ray AGNs at $z = 1$ tend to *avoid* big galaxies in the outskirts of yet more massive groups and clusters. They definitely avoid satellite galaxies in the $v_{\rm max} \gtrsim 300\,{\rm km\ s^{-1}}$ galaxy groups because otherwise we would find $1 - f = 0.3 - 0.6$.[17] Instead, the X-ray AGNs are preferentially located at the centers of distinct dark matter halos.

5.2. $V_{\rm min}$ *as a Function of Redshift*

Splitting our *Chandra*/Boötes AGN sample into 4 subsamples, ∼ 320 objects in each, we can measure the correlation length, r_0, as a function of redshift if we hold the slope of the correlation function fixed at the best-fit value obtained for the entire sample, $\gamma = 1.97$. The results are shown in Fig. 12. There is almost no change in r_0 over the redshift interval $z = 0.35 - 2.1$. A formal linear fit to the $r_0(z)$ measurements gives a change from $r_0 = 5.5\,h^{-1}$ Mpc at $z = 0.35$ to $r_0 \approx 7\,h^{-1}$ Mpc at $z = 2$. However, all the measurements are consistent with the average $r_0 = 6.27\,h^{-1}$ Mpc derived for the entire sample, so the trend with redshift is not significant.

Assuming further a fixed $f = 1$ at each z, as indicated by modeling of the redshift-space distortions in the entire sample, we can convert the best-fit values of r_0 at each redshift to the threshold circular velocity for the parent dark matter halos. The results are shown in Fig. 13. We find no detectable

[16] Hickox et al. (2009) quote a higher mass, $\sim 10^{13}\,h^{-1}\,M_\odot$ for an X-ray AGNs sample with the mean $\langle z\rangle = 0.51$, from which they measure $r_0 = 4.8\,h^{-1}$ Mpc. The main source of the difference, as explained in Conroy et al. (2008, see their p.1195), is a more accurate model for the matter power spectrum at galactic scales deployed in modern simulations such as those we use here.

[17] For example, there are 908 subhalos with $v_{\rm max} > 201\,{\rm km\ s^{-1}}$ located within 1650 $V_{\rm min} = 310\,{\rm km\ s^{-1}}$ halos, leading to $f = 0.65$.

trend of $V_{\rm min}$ or the corresponding mass threshold, $M_{\rm lim}$ (see Table 1), with redshift, either. This appears somewhat counterintuitive because in a flux-limited sample, such as ours, the objects at higher redshift have higher intrinsic luminosities, and we might expect them to be located in more massive dark matter halos. We note, however, that the studies of optically selected QSOs also indicate a weak or no trend of clustering length with the object luminosity (Croom et al. 2005; Shen et al. 2009). Clustering analysis of the SDSS quasars (Ross et al. 2009) shows mild or no evolution of the real-space correlation length at $z \lesssim 2$.

5.3. *Constraints on AGN Duty Cycle*

Having estimated the mass scale and therefore the space density of *Chandra*/Boötes AGNs, we can formally compute their duty cycle following the approach of Martini & Weinberg (2001). Under the simplifying assumption that the halo lifetime is approximately independent of mass, the probability for the AGN to be active is simply

$$P_{\rm active} = \frac{n_{\rm AGN}}{n_{\rm halo}}. \quad (19)$$

The limiting X-ray luminosity is ill-defined for our sample because the X-ray detection is extended down to very low limits in terms of the number of detected X-ray photons (≥ 4, see Kenter et al. 2005), and in this regime, a wide range of possible intrinsic intensities corresponds to the given number of photons (Kenter & Murray 2003). However, as a guide for the typical luminosity scale one can use the median $\log L_x$ reported in Table 1. With these caveats, the probabilities given by eq. 19 and reported in column (9) of Table 1 correspond to the probability for the dark matter halos with $v_{\rm max} > V_{\rm min}$ to host an AGN with the instantaneous soft-band X-ray luminosity of order $\langle \log L_x \rangle$ or above. Our results indicate that $P_{\rm active}$ generally declines with mean luminosity and/or redshift. Interestingly, our results indicate that AGNs are quite common at low redshifts — approximately 10% of dark matter halos with $v_{\rm max} > 270\,{\rm km\ s^{-1}}$ (or mass $M_{180} > 3.5 \times 10^{12}\,h^{-1}\,M_\odot$) host an AGN with a soft-band X-ray luminosity of $\sim 4 \times 10^{42}\,{\rm erg\ s^{-1}}$ or above.

6. DISCUSSION AND CONCLUSIONS

We measured the clustering properties of X-ray selected AGNs using a sample of 1282 sources with spectroscopic redshifts from the 9.3 deg^2 *Chandra* survey in the Boötes region — the most accurate such measurement to date. In agreement with previous studies of X-ray and optically selected AGNs, we find that the real-space correlation function can be approximated in the radial range $1-20\,h^{-1}$ comoving Mpc by a power law with a slope of $\gamma = 1.97 \pm 0.09$. The correlation length is $\approx 6.5\,h^{-1}$ Mpc, showing only weak trends with redshift at $z = 0.3 - 2$ (or with X-ray luminosity).

Matching the observed clustering properties of the *Chandra*/Boötes AGNs to those of dark matter halos in the high-resolution cosmological simulations, we find that the X-ray AGNs reside in halos with the maximum rotational velocity $\approx 310\,{\rm km\ s^{-1}}$, or with total masses $\sim 3.7 \times 10^{12}\,h^{-1}\,M_\odot$, also with no detectable redshift trend. The lack of a redshift or luminosity dependence of the AGN clustering is inconsistent with the scenarios in which the AGN luminosities in the active state are similar fractions of the Eddington luminosity. However, it can be explained in the scenario in which the AGN activity is triggered by major mergers of gas-rich galaxies, and the instantaneous luminosity passes through many levels after each trigger (Hopkins et al. 2006).

Our results reveal another interesting aspect of the AGN clustering which was predicted in Hopkins et al. (2008). The redshift measurements in our sample are sufficiently accurate to detect peculiar motions of objects in excess of $\sim 100\,{\rm km\ s^{-1}}$. The comparison of the two-point correlation functions projected on the line of sight and on the sky plane reveals no signatures of the redshift-space distortions, which allows us to put limits on the fraction of AGNs located in the satellite subhalos *within* the host dark matter halos. We find that the X-ray AGNs are predominantly located in the central galaxies of the host dark matter halos and tend to *avoid* satellite galaxies. Quantitatively, we limit the fraction of AGNs in non-central galaxies to be < 0.09 at the 95% CL, less than that expected from the abundance of satellite subhalos found in the numerical simulations (§ 5.1). The central locations of the quasar host galaxies are expected in the trigger model because mergers of equally-sized galaxies preferentially occur at the centers of dark matter halos (Hopkins et al. 2008).

Finally, we compared the number densities of the *Chandra*/Boötes AGNs to that of the dark matter halos with the mass corresponding to the AGN clustering amplitude. We find that the fraction of halos with active X-ray AGNs decreases with increasing z — and, correspondingly, with L_x — probably reflecting the lower probability for an object to have a higher instantaneous luminosity. At the lowest redshifts in our sample, *Chandra* probes such a low luminosity that X-ray AGNs become quite common. At $z = 0.37$, the *Chandra*-detected sources are located in more than 10% of the dark matter halos with $v_{\rm max} > 270\,{\rm km\ s^{-1}}$ or $M > 3.55 \times 10^{12}\,h^{-1}\,M_\odot$.

This work was supported by the Smithsonian Institution and *NASA* through contracts NAS8-39073 and NAS8-03060 (CXC). AK is supported by the NSF grant AST-0708154, by NASA grant NAG5-13274, and by Kavli Institute for Cosmological Physics at the University of Chicago through grant NSF PHY-0551142 and an endowment from the Kavli Foundation. We thank O. Gnedin and A. Franceschini for useful discussions and comments.

Facilities: Chandra, MMT.

REFERENCES

Angulo, R. E. & White, S. D. M. 2010, MNRAS, 405, 143
Bardeen, J. M., Bond, J. R., Kaiser, N., & Szalay, A. S. 1986, ApJ, 304, 15
Berlind, A. A. & Weinberg, D. H. 2002, ApJ, 575, 587
Berlind, A. A., et al. 2003, ApJ, 593, 1
Bond, J. R. & Efstathiou, G. 1984, ApJ, 285, L45
Brand, K., et al. 2006, ApJ, 641, 140
Cappelluti, N., Böhringer, H., Schuecker, P., Pierpaoli, E., Mullis, C. R., Gioia, I. M., & Henry, J. P. 2007, A&A, 465, 35
Cappi, M., et al. 2001, ApJ, 548, 624
Colín, P., Valenzuela, O., & Klypin, A. 2006, ApJ, 644, 687
Conroy, C., Shapley, A. E., Tinker, J. L., Santos, M. R., & Lemson, G. 2008, ApJ, 679, 1192
Conroy, C., Wechsler, R. H., & Kravtsov, A. V. 2006, ApJ, 647, 201
Croom, S. M., et al. 2005, MNRAS, 356, 415
Davis, M. & Peebles, P. J. E. 1983, ApJ, 267, 465
Eisenstein, D. J. & Hu, W. 1998, ApJ, 496, 605
Fabricant, D., et al. 2005, PASP, 117, 1411
Ferrarese, L. & Ford, H. 2005, Space Sci. Rev., 116, 523

Gebhardt, K., et al. 2000, ApJ, 539, L13
Gilli, R., et al. 2005, A&A, 430, 811
Gilli, R., et al. 2009, A&A, 494, 33
Hickox, R. C., et al. 2009, ApJ, 696, 891
Hogg, D. W. 1999, ArXiv Astrophysics e-prints
Hopkins, P. F., Hernquist, L., Cox, T. J., Di Matteo, T., Robertson, B., & Springel, V. 2006, ApJS, 163, 1
Hopkins, P. F., Hernquist, L., Cox, T. J., & Kereš, D. 2008, ApJS, 175, 356
Hu, W. & Kravtsov, A. V. 2003, ApJ, 584, 702
Jenkins, A., Frenk, C. S., White, S. D. M., Colberg, J. M., Cole, S., Evrard, A. E., Couchman, H. M. P., & Yoshida, N. 2001, MNRAS, 321, 372
Kaiser, N. 1984, ApJ, 284, L9
Kaiser, N. 1987, MNRAS, 227, 1
Kenter, A., et al. 2005, ApJS, 161, 9
Kenter, A. T. & Murray, S. S. 2003, ApJ, 584, 1016
Klypin, A., Gottlöber, S., Kravtsov, A. V., & Khokhlov, A. M. 1999, ApJ, 516, 530
Komatsu, E., et al. 2010, ArXiv e-prints
Koulouridis, E. & Plionis, M. 2010, ApJ, 714, L181
Kravtsov, A. V., Berlind, A. A., Wechsler, R. H., Klypin, A. A., Gottlöber, S., Allgood, B., & Primack, J. R. 2004, ApJ, 609, 35
Kravtsov, A. V. & Klypin, A. A. 1999, ApJ, 520, 437
Landy, S. D. & Szalay, A. S. 1993, ApJ, 412, 64
Ma, C. & Fry, J. N. 2000, ApJ, 543, 503
Magorrian, J., et al. 1998, AJ, 115, 2285
Martini, P., Kelson, D. D., Kim, E., Mulchaey, J. S., & Athey, A. A. 2006, ApJ, 644, 116
Martini, P. & Weinberg, D. H. 2001, ApJ, 547, 12
Mo, H. J. & White, S. D. M. 1996, MNRAS, 282, 347
Molnar, S. M., Hughes, J. P., Donahue, M., & Joy, M. 2002, ApJ, 573, L91
Murray, S. S., et al. 2005, ApJS, 161, 1
Nagai, D. & Kravtsov, A. V. 2005, ApJ, 618, 557
Oegerle, W. R. & Hill, J. M. 2001, AJ, 122, 2858
Padmanabhan, N., White, M., Norberg, P., & Porciani, C. 2009, MNRAS, 397, 1862
Peacock, J. A. & Smith, R. E. 2000, MNRAS, 318, 1144
Peebles, P., The Large Scale Structure of the Universe (Princeton University Press, 1980)
Peebles, P. J. E. 1973, ApJ, 185, 41
Plionis, M., Rovilos, M., Basilakos, S., Georgantopoulos, I., & Bauer, F. 2008, ApJ, 674, L5
Ross, N. P., et al. 2009, ApJ, 697, 1634
Scoccimarro, R., Sheth, R. K., Hui, L., & Jain, B. 2001, ApJ, 546, 20
Seljak, U. 2000, MNRAS, 318, 203
Shen, Y., et al. 2009, ApJ, 697, 1656
Sheth, R. K. & Tormen, G. 1999, MNRAS, 308, 119
Tasitsiomi, A., Kravtsov, A. V., Wechsler, R. H., & Primack, J. R. 2004, ApJ, 614, 533
Tinker, J. L. 2007, MNRAS, 374, 477
Tinker, J. L., Weinberg, D. H., & Zheng, Z. 2006, MNRAS, 368, 85
Vikhlinin, A. & Forman, W. 1995, ApJ, 455, L109
Vikhlinin, A., et al. 2009, ApJ, 692, 1060
White, M., Hernquist, L., & Springel, V. 2001, ApJ, 550, L129
Zehavi, I., et al. 2002, ApJ, 571, 172
Zehavi, I., et al. 2005, ApJ, 621, 22
Zheng, Z., et al. 2005, ApJ, 633, 791

APPENDIX

COSMOLOGY-DEPENDENT SCALINGS OF THE MODEL CORRELATION FUNCTION

Using the simulation outputs directly has many advantages over the analytic HOD model in testing different models of populating the dark matter halos with astronomical sources. However, there is an important disadvantage. The simulations are performed for a certain combination of the cosmological parameters, which may or may not match the currently favored cosmological model. For example, the numerical simulations we use in this work were performed assuming a high value of the power spectrum normalization, $\sigma_8 = 0.9$ at $z = 0$. This results in a slightly incorrect prediction of the correlation amplitude for halos of a given mass, and thus slightly biases the derived parameters of the AGN population model.

Fortunately, as we discuss below, the simulation-based models can be easily adjusted to the "correct" cosmology by simply rescaling the halo masses by a small factor. A more elaborate procedure is described by Angulo & White (2010) who show that even the raw simulation outputs can be rescaled to the correct cosmology.

Basics

The correlation function of objects with mass M at a given redshift, z, can be written as

$$\xi(r, M) = b^2(M)\,\xi_{\rm DM}(r), \tag{A1}$$

where $b(M)$ is the bias factor for halos with mass M, and $\xi_{\rm DM}(r)$ is the correlation function of all dark matter particles. Since we consider the correlation function measurements at the separations bracketing $8\,h^{-1}$ Mpc, we can assume that with sufficient accuracy, $\xi_{\rm DM}(r) \propto \sigma_8^2(z) = \sigma_{8,0}^2 D(z)^2$, where $D(z)$, is the linear perturbations growth factor for the given cosmology.

The bias factor, $b(M)$, is, in turn, a function of the linear perturbation amplitude at the mass scale M, $b(M) = b(\sigma(M))$ (Kaiser 1984; Mo & White 1996; Sheth & Tormen 1999). Therefore, we conclude that the dependence of the correlation function model on cosmology is through σ_8, $D(z)$, and $\sigma(M)$.

Scaling for $\sigma(M)$

The scales corresponding to the galaxy-sized objects are sufficiently small that the slope of the matter power spectrum and hence the mass dependence in $\sigma(M)$ is insensitive to the underlying cosmology (Bardeen et al. 1986). In a fairly broad range of parameters around the "concordance" cosmological model, we find that $\sigma(M)$ computed with the full transfer function (e.g., Eisenstein & Hu 1998) can be approximated as $\sigma(M) = A \times M^{-0.16}$ in the mass range $10^{12} - 10^{13}\,M_\odot$. The amplitude, A, of this power law approximation scales with cosmology as

$$A \propto \sigma_8 \times D(z) \times s(\Omega_M, h, ...). \tag{A2}$$

In this equation, the factor $s(\Omega_M, h, ...)$ represents the correction for the different power spectrum shapes in different cosmologies (it is mostly a function of the product $\Omega_M h$, see Bond & Efstathiou 1984). We neglected such a factor in $\xi_{DM}(r)$ because we consider the cosmological models in which the perturbations are normalized by σ_8, the fluctuation amplitude at approximately the midpoint of the observed range. However, the scale corresponding to galaxy-sized objects for which $\sigma(M)$ has to be computed, is sufficiently far from $8\,h^{-1}$ Mpc so that the correction can be important. For example, we find that $s_1/s_2 = 1.03$ for the flat ΛCDM cosmologies with $(\Omega_M, h) = (0.3, 0.7)$ and $(0.268, 0.71)$ (more power in the high-Ω_M case).

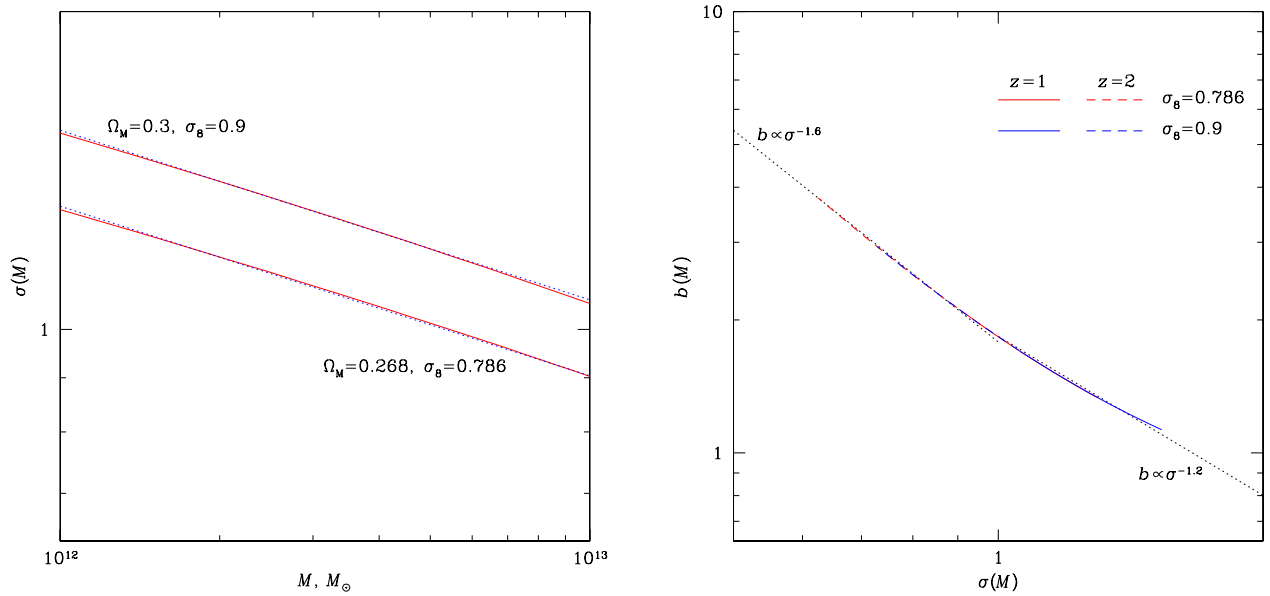

FIG. 14.— Cosmological functions $\sigma(M)$ and $b(M)$ computed for two different flat ΛCDM cosmologies, $(\Omega_M, \sigma_8) = (0.3, 0.9)$ and $(0.268, 0.786)$. The left panel shows $\sigma(M)$ computed at $z = 1$ (solid lines) and the power law approximations, $\sigma \propto M^{-0.16}$ (dotted lines). In the right panel, the linear bias, $b(M)$, is plotted as a function of $\sigma(M)$ for the same two cosmologies and for $z = 1$ and 2 (the mass range is $M = 10^{12} - 10^{13}$ as in the left panel).

Scaling for $b(\sigma(M))$

The key notion for our computation is that the halos with $M = 10^{12} - 10^{13}$ are "rare" objects at $z \gtrsim 1$ ($\sigma(M) \sim 1$ or less) with high bias factors strongly dependent on $\sigma(M)$. The bias as a function of $\sigma(M)$ can be computed using the Sheth & Tormen (1999) approximation:

$$b = 1 + \frac{a\,\delta_c^2/\sigma^2 - 1}{\delta_c} + \frac{2p}{\delta_c\left[1 + (a\,\delta_c^2/\sigma^2)^p\right]} \tag{A3}$$

with parameters $a = 0.75$ and $p = 0.3$ (adopted from Hu & Kravtsov 2003, see their page 704), and $\delta_c = 1.69$ is the threshold for spherical collapse in a matter-dominated universe. The bias computed from this equation for the two cosmologies and two different redshifts is shown in the right panel of Fig. 14. For the mass range $10^{12} - 10^{13}\,M_\odot$, the bias can be approximated as $b \propto \sigma^{-1.6}$ at $z = 2$ and $b \propto \sigma^{-1.2}$ at $z = 1$.

Scaling of Mass Derived from the Two-Point Correlation Functions

Since $\sigma(M)$ is a weak function of mass, the linear bias is also a weak function of M, $b(M) \propto M^{0.2-0.25}$ in our mass range. However, $\sigma(M)$ scales linearly with σ_8, and the bias also shows a strong dependence on this parameter, $b \propto \sigma_8^{-1.6\ldots-1.2}$. For the correlation function of halos, we have $\xi = \xi_{\rm DM}\,b^2 \propto \sigma_8^{-1.2} \ldots \sigma_8^{-0.4}$. We, therefore, arrive at a somewhat counterintuitive conclusion — the amplitude of the correlation function of galaxy-sized objects at high z is *lower* for models with high values of σ_8 because of a strong dependence of the linear bias on the underlying amplitude of the density perturbations, $\sigma(M)$.

When we determine the mass scale of objects from their correlation function, we effectively solve the equation

$$\xi_{DM}\,b^2(M) \propto \sigma_8^2\,D(z)^2\,b^2(M) = C, \tag{A4}$$

where C is a constant provided by the data. Inserting the scalings derived above, we can rewrite this as

$$\sigma_8^2\,D(z)^2\left[\sigma_8\,D(z)\,s\,M^{-0.16}\right]^{-2\alpha} = C \tag{A5}$$

where we assume that $b(M)$ is approximated as a power law of $\sigma(M)$, $b \propto \sigma^{-\alpha}$ (e.g., $\alpha = -1.6$ for our mass range and $z = 2$). From here we have,

$$M^{0.16} \propto [\sigma_8\,D(z)]^{\alpha-1}\;s^\alpha \tag{A6}$$

If we scale the object masses by this equation, the halo clustering properties in the two different cosmologies will be very similar.

As an example, consider the scaling between the cosmology used in the simulations, $\Omega_M = 0.3$, $h = 0.7$, $\sigma_8 = 0.9$, and the galaxy cluster-normalized best-fit model from Vikhlinin et al. (2009), $\Omega_M = 0.268$, $h = 0.715$, $\sigma_8 = 0.786$. At $z = 1.03$, the median redshift of our *Chandra*/Boötes X-ray sample of AGNs, $D(z) = 0.616$ and 0.604 for $\Omega_M = 0.268$ and 0.3, respectively. The shape factors, s, are 1 and 1.03 for $\Omega_M = 0.268$ and 0.3, respectively. Inserting into eq. A6, we find that the masses which would be derived in the $\Omega_M = 0.268$, $\sigma_8 = 0.786$ cosmology are a factor of 1.45 lower than those derived using the correlation function models obtained directly from the simulation outputs.

At $z = 2$, $D(z) = 0.284$ and 0.277 for $\Omega_M = 0.268$ and 0.3, respectively. Using eq. [A6], we find that the object masses should be scaled down by factors $1.7 \ldots 2$ for $\alpha = 1.4 \ldots 1.6$ (the range of slopes for the $z = 2$ objects, see Fig. 14).

Scaling for the Number Density of Objects

A related question is how to scale the *number density* of objects with the given clustering properties. In many situations, it should be possible to use a mass function model (e.g., the one from Sheth & Tormen 1999) for such a scaling. However, for galaxy-sized objects it is possible to derive a simple scaling for the number density.

Jenkins et al. (2001) show that the mass function of halos can be written in a standard form,

$$\frac{dn}{dM} = B \times \frac{1}{M^2} \frac{d\ln\sigma^{-1}}{d\ln M} \varphi(\sigma), \tag{A7}$$

where B is a constant, $\sigma(M)$ is the linear perturbations amplitude on scale M, and $\varphi(\sigma)$ is a "universal" function. For the Sheth & Tormen (1999) model,

$$\varphi(\sigma) = 0.32 \sqrt{\frac{2a}{\pi}} \left[1 + \left(\frac{\sigma^2}{a\,\delta_c^2}\right)^p\right] \frac{\delta_c}{\sigma} \exp\left(-\frac{a\,\delta_c^2}{2\,\sigma^2}\right) \tag{A8}$$

where the parameters a and p are the same as in the expression for the linear bias (eq. [A3]). For $\sigma \lesssim 1$, as is the case for our galaxy-sized objects, the Sheth & Tormen f is a slowly varying function of σ which can be approximated as

$$\varphi(\sigma) \simeq 0.65 + \ln\sigma \tag{A9}$$

Inserting this into eq. [A7] and taking into account that $\sigma(M) \propto M^{-0.16}$ (see above), we have for the number density of objects above a mass threshold $M_{\rm lim}$,

$$N = \int_{M_{\rm lim}}^{\infty} B \times \frac{0.16}{M^2} \left[0.65 + \ln\sigma_{\rm lim} - 0.16\ln(M/M_{\rm lim})\right] dM \propto M_{\rm lim}^{-1} \left(0.49 + \ln\sigma_{\rm lim}\right) \tag{A10}$$

where $\sigma_{\rm lim} = \sigma(M_{\rm lim})$. Now we can take into account that the limiting mass is found from the condition A4 (so that the clustering properties match those observed). If bias is approximated as a power law of σ, $b(M) \propto \sigma(M)^{-\alpha}$ (Fig. 14),

$$\sigma_{\rm lim} \propto [\sigma_8 D(z)]^{1/\alpha}\,. \tag{A11}$$

Equations A10, A11, and A6 provide the scaling for the number density of isolated halos whose clustering properties match the observations. Assuming that the relative number density of satellite and main halos is not very sensitive to the underlying cosmology, the same scaling can be applied to any other type of halos.

In summary, we suggest the following procedure. One takes the simulation outputs and adjusts the mass threshold, $M_{\rm lim}$ so that the correlation function amplitude derived for the halos with mass above this threshold matches that observed. One then measures the number density, N, of such halos in the simulation box. To convert these quantities to the desired cosmology, one uses eq. A6 to scale $M_{\rm lim}$ and equations A10, A11, and A6 for the number density. For example, we found for the *Chandra*/Boötes AGNs $V_{\rm min} = 310\,{\rm km\ s^{-1}}$, which corresponds to $M_{\rm lim} = 3.7 \times 10^{12}\,h^{-1}\,M_\odot$. This corresponds to $\sigma_{\rm lim} = 1.25$ at $z = 1$. To adjust these results from the $(\Omega_M, \sigma_8) = (0.3, 0.9)$ to $(0.268, 0.786)$ cosmology, we need to scale $M_{\rm lim}$ by a factor of 0.69, and increase the number density by a factor of 1.2 (the $M_{\rm lim}^{-1}$ factor is partially compensated for by the change in $\ln\sigma_{\rm lim}$).